Available online at www.sciencedirect.com

SciVerse ScienceDirect

Ceramics International 39 (2013) 5125–5136

CERAMICS INTERNATIONAL

www.elsevier.com/locate/ceramint

Reaction mechanisms of synthesis and decomposition of fluorapatite–zirconia composite nanopowders

Bahman Nasiri-Tabrizi*, Abbas Fahami

Materials Engineering Department, Najafabad Branch, Islamic Azad University, Najafabad, Isfahan, Iran

Received 16 November 2012; received in revised form 30 November 2012; accepted 1 December 2012
Available online 10 December 2012

Abstract

The reaction mechanisms of formation and decomposition of fluorapatite – zirconia composite nanopowders were investigated after the mechanochemical process and subsequent thermal treatment. Experimental results indicated that formation of fluorapatite – zirconia composite nanopowders proceeded in several steps. In the first stage, phosphoric acid formed immediately upon addition of phosphorous pentoxide to the reaction mixture. Afterwards, anhydrous dicalcium phosphate was generated as a result of reaction between reagents with phosphoric acid. The synthesis progressed by the formation of the stoichiometrically deficient hydroxyfluorapatite – zirconia composite at milling times between 5 and 15 min. Ultimately, the fluorapatite – zirconia composite nanopowder was obtained after 300 min of milling. Results revealed that the annealing process led to a decomposition of fluorapatite to tricalcium phosphate and calcium fluoride, and to the transformation of monoclinic zirconia to the tetragonal form. Field emission scanning electron microscope observations showed that the milled sample was composed of fine particles with a mean particle size of about 45 nm after 300 min of milling. Besides, the mean particle size increased progressively due to crystal growth in the temperature range above 900 °C. According to the gained data, reaction mechanism steps were proposed to clarify the reactions occurring during the above-mentioned solid state process.

Keywords: Reaction mechanism; Mechanochemical; Fluorapatite – zirconia; Heat treatment

1. Introduction

Hydroxyapatite (HAp, $Ca_{10}(PO4)_6(OH)_2$) seems to be the most appropriate ceramic material for artificial bone and tooth applications owing to its excellent biocompatibility and bioactivity [1]. However, HAp has intrinsically high dissolution rate in a biological system, poor corrosion resistance in an acidic environment and poor chemical stability at high-temperature [2,3]. Hydroxyapatite as the main inorganic phase of human hard tissue can be doped with different quantities of cations and anions such as Na^+, K^+, Mg^{2+}, CO_3^{2-}, SO_4^{2-} and F^{1-} [4]. These substitutions in apatite lattice can affect the lattice parameters, crystallinity, dissolution kinetics and other physical properties [5]. Among them, F^{1-} ion plays a key role due to its influence on the physical and biological properties of HAp. F^{1-} prevents dental caries in an acidic environment and promotes the mineralization and crystallization of calcium phosphate in the bone forming process [4].

On the other hand, the incorporation of bioinert ceramics into calcium phosphate-based materials has shown significant improvement in structural features as well as mechanical properties. An ideal reinforcing material for the calcium phosphate-based composites, which satisfies all of requirements, has not yet been found. However, several attempts have been made to develop HAp- and fluoridated hydroxyapatite (FHAp, $Ca_{10}(PO_4)_6(OH)_{2-x}F_x$)-based composites [6–11]. These studies revealed that two major common phenomena ordinarily occur that consist dissociation of HAp to tricalcium phosphate (α/β-TCP) and interfacial reactions between HAp and reinforcement ceramic phase, which can lead to the formation of $CaZrO_3$ and $CaTiO_3$. Among the second phases, ZrO_2 has been studied extensively because of its relatively higher mechanical strength and toughness [7–9]. However, the addition of ZrO_2 results

*Corresponding author. Tel.: +98 3114456551; fax: +98 3312291008.
E-mail address: bahman_nasiri@hotmail.com (B. Nasiri-Tabrizi).

0272-8842/$ - see front matter © 2012 Elsevier Ltd and Techna Group S.r.l. All rights reserved.
http://dx.doi.org/10.1016/j.ceramint.2012.12.008

in lowering the decomposition temperature of microcrystalline HAp- and FHAp-based composites below the sintering temperature which causes an adverse influence on the mechanical properties [12]. Hence, control over the characteristics of composite structures is a challenging act. Our recent studies suggest that fluorapatite−zirconia (FAp–ZrO_2) composite nanopowders can be generated by solid state process which include dry mechanochemical technique (to obtain FAp–ZrO_2 composite nanopowders) and thermal annealing process (for recovery of crystallinity degree of composite powders) [13]. High efficiency of this procedure proposes an appropriate approach to produce commercial amount of FAp–ZrO_2 composite nanopowders.

In this paper, reaction mechanisms of formation and decomposition of fluorapatite−zirconia composite nanopowders were investigated after mechanochemical process and subsequent thermal treatment as the second stage of experiment. For this aim, structural and morphological features of powder mixture in the absence and presence of monoclinic zirconia were evaluated by X-ray diffraction (XRD), Fourier transform infrared spectroscopy (FT-IR), energy dispersive X-ray spectroscopy (EDX), scanning electron microscopy (SEM) and field emission scanning electron microscopy (FE-SEM). Based on the obtained data, formation of fluorapatite–zirconia composite nanopowders progressed in several steps.

2. Materials and methods

Calcium oxide (CaO, Merck), phosphorous pentoxide (P_2O_5, Merck), calcium fluoride (CaF_2, Merck) and monoclinic zirconia (*m*-ZrO_2, Merck) were used as starting reagents. Details of the mechanochemical process have been presented elsewhere [13]. In summary, mechanosynthesis was performed in a planetary ball mill using Zirconia balls (20 mm in diameter) and sealed cylindrical polyamide-6 vials (vol. 125 ml). The weight ratio of ball-to-powder was 20:1. The objectives of milling were twofold: to synthesize nanocrystalline FAp according to reaction (1) and to generate a fine homogeneous FAp–ZrO_2 composite powders in accordance with reaction (2).

$$9CaO + 3P_2O_5 + CaF_2 \rightarrow Ca_{10}(PO_4)_6F_2 \quad (1)$$

$$9CaO + 3P_2O_5 + CaF_2 + m\text{-}ZrO_2 \rightarrow Ca_{10}(PO_4)_6F_2 + m\text{-}ZrO_2 \quad (2)$$

For the first aim, the initial powders including CaO, P_2O_5 and CaF_2 were ground on a planetary ball mill with the stoichiometric proportionality between the materials given in the reaction (1). For the second object, the distinct amount of *m*-ZrO_2 (5 wt%) mixed with CaO, P_2O_5, and CaF_2 according to the reaction (2). Milling was carried out for 5, 15, 30, and 300 min. The experimental outcomes in the absence and presence of 5 wt% *m*-ZrO_2 were named as 0ZFA and 5ZFA, respectively. Subsequently, the composite powders were filled in quartz boat, and then annealed for 1 h under atmospheric pressure in the range of 600–1300 °C. The heating rate from room temperature up to the desired temperature was fixed at 10 °C min^{-1}.

Phase analyses of products were determined by X-ray diffraction (Philips X-ray diffractometer (XRD), *Cu-K*$_\alpha$ radiation, 40 kV, 30 mA and 0.02° s^{-1} step scan). XRD graphs were recorded in the interval $20° \le 2\theta \le 60°$ at scan speed of 1°/min. "*PANalytical X'Pert HighScore*" software was also utilized for the analysis of different peaks. The gained patterns were compared to standards compiled by the Joint Committee on Powder Diffraction and Standards (JCPDS), which involved card #15-0876 for FAp, #037-1497 for CaO, #035-0816 for CaF_2, #01-1079 for $Ca(OH)_2$, #05-0318 for P_2O_5, #09-0169 for β-TCP, #037-1484 for *m*-ZrO_2 and #017-0923 for *t*-ZrO_2. Crystallite size and lattice strain of the samples were determined by using the XRD data according to the following equations [13,14]:

$$D = \frac{K\lambda}{(b_{obs} - b_{std})(b\cos\theta)} \quad (I)$$

$$E^2 = \frac{(b_{obs}{}^2 - b_{std}{}^2)}{(4\tan\theta)^2} \quad (II)$$

where b (in rad), K, λ, D, E and θ are the structural broadening, shape coefficient (value between 0.9 and 1.0), the wavelength of the X-ray used (0.154056 nm), crystallite size, lattice strain and the Bragg angle (deg.), respectively.

On the other hand, the relation between lattice spacing (d) and lattice parameters (a, b, and c) of the hexagonal structures (FAp and the FAp in the composites) was shown as

$$\frac{1}{d^2} = \frac{4}{3}\frac{h^2 + hk + k^2}{a^2} + \frac{l^2}{c^2} \quad (III)$$

where h, k, l are the Miller indices of the reflection planes. The (0 0 2) and (3 0 0) reflections were chosen for the lattice parameters calculation [15].

Moreover, volume V of the hexagonal unit cell was determined by the following formula [9]:

$$V = 2.589a^2c \quad (IV)$$

The lattice parameter change in the tetragonal zirconia (*t*-ZrO_2) was investigated using XRD data. The (1 1 1) and (2 2 0) reflections corresponding to the *t*-ZrO_2 were chosen for the (a) parameter determination [16].

$$\frac{1}{d^2} = \frac{h^2 + k^2}{a^2} + \frac{l^2}{c^2} \quad (V)$$

where d is the lattice spacing, h, k, l are the Miller indices, and a and c are the lattice parameters in a tetragonal crystal.

The percentage of volume fraction of β-TCP present in all the heat treated samples was determined using semi-quantitative XRD by comparing the peaks of FAp (2 1 1) and β-TCP (0 2 1 0) from XRD patterns [17]

$$TCP = \frac{I_{TCP\ (0\ 2\ 1\ 0)}}{I_{TCP\ (0\ 2\ 1\ 0)} + I_{FAp\ (2\ 1\ 1)}} \quad (VI)$$

Here, I_{TCP} and I_{FAp} represent the XRD normalized integrated intensity values of β-TCP (0 2 1 0) and FAp (2 1 1) reflections.

Fourier transform infrared (FT-IR, Model 680 Plus, JASCO) spectroscopy was also used to characterize the products. The transmittance spectroscopy was recorded in the range 4000–400 cm^{-1} at 2 cm^{-1} resolution by 16 scans. Energy dispersive X-ray spectroscopy (EDX) which was coupled with SEM (SERON AIS-2100) was utilized for semi-quantitative examination of the samples (voltage used for EDX equal to 20 kV). Morphological characteristics of the nanopowders were examined on a field emission scanning electron microscope (FE-SEM Hitachi S1831) that operated at the acceleration voltage of 15 kV. For this purpose, the gained powders were coated with gold for more electronic conduction.

3. Results and discussion

3.1. XRD analysis

3.1.1. Phase evolution

Fig. 1 shows the XRD patterns of CaO, P_2O_5 and CaF_2 powder mixture in the absence of *m*-ZrO_2 (0ZFA) before and after mechanical activation for different milling times. Phosphoric acid (H_3PO_4) formed immediately upon addition of P_2O_5 to the reaction mixture due to very high hydrophilic of P_2O_5. Accordingly, characteristic peaks of P_2O_5 could not be observed in XRD profiles. On the other hand, CaO is unstable and can be transformed to calcium carbonate ($CaCO_3$) or to calcium hydroxide ($Ca(OH)_2$) in air as shown in Fig. 1. After 5 min of milling, the appearance of peaks around $2\theta = 31–34^\circ$ confirmed the formation of FAp phase. In addition, five intense peaks were observed in XRD pattern corresponding to CaO and $Ca_2P_2O_7$. Similarly, these phases were presented in the XRD patterns of samples milled for 15 and 30 min. This suggests that the mechanochemical reaction between CaO and H_3PO_4 caused the formation of $Ca_2P_2O_7$ in the final product synthesized after 5, 15 and 30 min of milling according to reaction (3).

$$2CaO + 2H_3PO_4 \rightarrow Ca_2P_2O_7 + 3H_2O,$$
$$\Delta G_{298\ K} = -398.815\ kJ, \quad \Delta H_{298\ K} = -368.469\ kJ \qquad (3)$$

The products after 5, 15 and 30 min of milling had the Ca/P ratio lower than stoichiometry value (Ca/P = 1.67) as a result of $Ca_2P_2O_7$ formation during milling. Nonetheless, the main product of the mechanochemical process was FAp. When the mechanical activation time was extended to 300 min, all the peaks corresponding to $Ca_2P_2O_7$ and CaO have disappeared and only those belonging to FAp were detectable. According to Fig. 1, the intensity decreasing rate of each starting material differed. By comparing the relative intensities of peaks corresponding to CaF_2 and CaO, it was found that the peak intensity of CaO decreased relatively slowly, while CaF_2 completely vanished after 5 min of milling. Eventually, a single phase

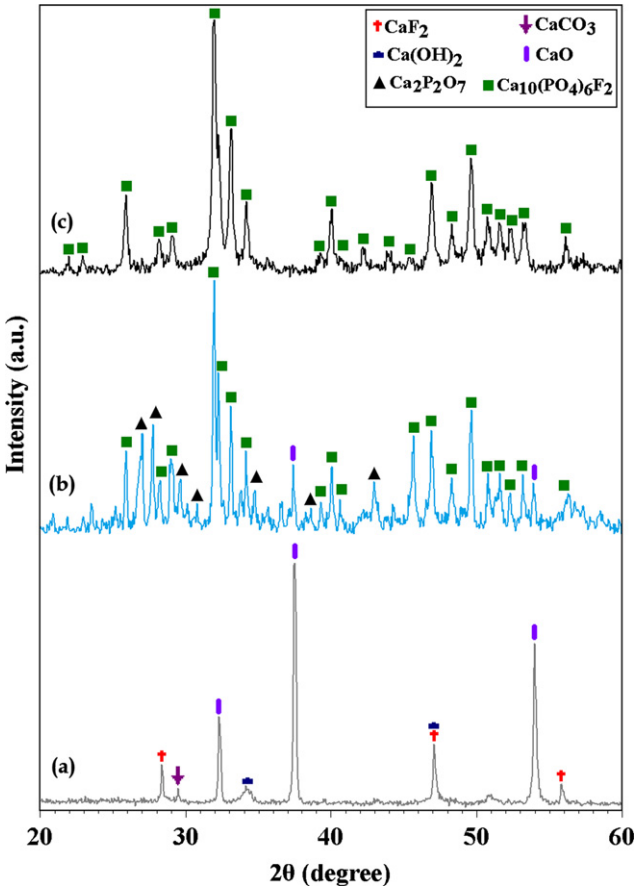

Fig. 1. XRD patterns of CaO, P_2O_5 and CaF_2 powder mixture in the absence of *m*-ZrO_2 (0ZFA) (a) before and after mechanical activation for different milling times, (b) 5 min and (c) 300 min.

FAp with no impurity phase was formed after 300 min of milling.

Fig. 2 shows the XRD patterns of CaO, P_2O_5 and CaF_2 powder mixture in the presence of 5 wt% *m*-ZrO_2 (5ZFA) before and after milling for different times of milling. As it can be seen in Fig. 2, after 5 min of milling the phase compositions were FAp and *m*-ZrO_2 with a trace of CaO. After 15 and 30 min of milling, similar to previous sample, the main product of mechanochemical reaction was FAp-ZrO_2 composite with a small amount of CaO. This suggests that CaO was still present in the 5ZFA samples after 5, 15 and 30 min of milling. It should be mentioned that $Ca_2P_2O_7$ was not found in the 5ZFA sample after different milling times. Therefore, it seems that the adding of 5 wt% *m*-ZrO_2 to the powder mixture can prevent the formation of $Ca_2P_2O_7$ as an extra phase. By increasing the milling duration up to 300 min, all the peaks related to CaO had completely disappeared and FAp–5 wt% *m*-ZrO_2 composite with no impurity phase was formed.

The thermal annealing process was served to investigate the effect of thermal activation on the phase transformations of FAp-ZrO_2 composite nanopowders. The XRD graphs of FAp–ZrO_2 composite nanopowders after thermal annealing process at 900, 1100 and 1300 °C for 1 h are

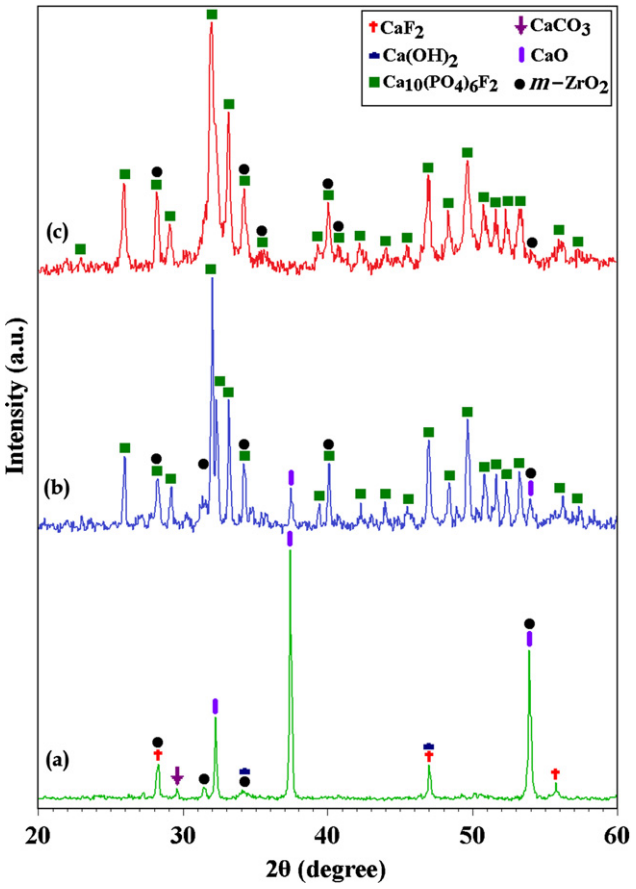

Fig. 2. XRD patterns of CaO, P_2O_5 and CaF_2 powder mixture in the presence of 5 wt% m-ZrO_2 (5ZFA) (a) before and after milling for different times of milling, (b) 5 min and (c) 300 min.

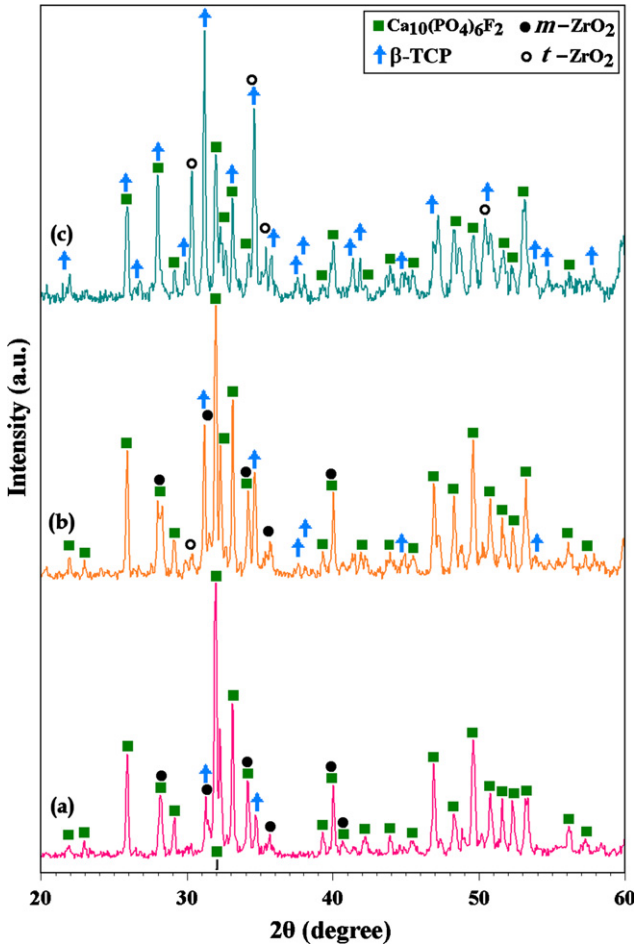

Fig. 3. XRD graphs of FAp–ZrO_2 composite nanopowders after thermal treatment at (a) 900, (b) 1100, and (c) 1300 °C.

shown in Fig. 3. Based on our previous result, poor crystalline apatite phase was formed at 600 °C [13]. From Fig. 3, it was verified the existence of FAp and m-ZrO_2 phases together with minor β-TCP phase after the annealing at 900 °C. This indicates that the partial decomposition of FAp occurs even at 900 °C in the presence of zirconia. XRD profile of composite nanopowders after heating at 1100 °C showed the formation of FAp, β-TCP, and m-ZrO_2 as major phases and the commencement of t-ZrO_2 phase formation. When the composite powders heat treated at 1300 °C, the distinctive peaks of stronger β-TCP were noticeably observed with moderate strong FAp peaks. It has been reported [11,14] that the final microstructure TCP will contain β or α-TCP depending on their cooling rate. Rapid cooling from sintering temperature causes to α-TCP phase only, whereas slow furnace cooling leads to β-TCP phase only. Any moderate cooling rate, between these two results mixed phase of both β and α-TCP. Hence, in present study the slow furnace cooling rate leads to the generation of β-TCP phase in heat treated samples. On the other hand, at temperatures higher than 1100 °C the process of phase transition of the m-ZrO_2 into the t-ZrO_2 took place. This phenomenon was accompanied by the disappearance of reflections originating from the m-ZrO_2 at $2\theta = 28.17°$ and 31.24°, and the appearance of peaks at $2\theta = 30.31°$ and 34.58° corresponding to the t-ZrO_2. This transformation is presumably due to the formation of CaF_2–ZrO_2 solid solution [18]. Fig. 4 displays the magnified XRD region between $2\theta = 29°$ and 34° and the volume fraction of β-TCP as a function of annealing temperature. According to this figure, with increasing of annealing temperature, the β-TCP (0 2 1 0) peak began to be appeared at 900 °C. For the sample annealed at 1100 °C, there was a weak peak (0 2 1 0), which became more intense as annealing temperature approaches at 1300 °C. Conversely, intensity of the FAp (2 1 1) peak decreased while the annealing temperature increased up to 1300 °C. Thus, a considerable degree of FAp decomposition observed in the composite nanopowders after thermal annealing process at 1300 °C. This suggests that in the composite structure, the volume fraction of β-TCP enhanced as a result of FAp decomposition during heating at $\geq$ 900 °C.

3.1.2. Crystallite size and lattice strain

Fig. 5 shows the structural features of specimens after milling and subsequent thermal treatment. For 0ZFA samples (Fig. 5a),

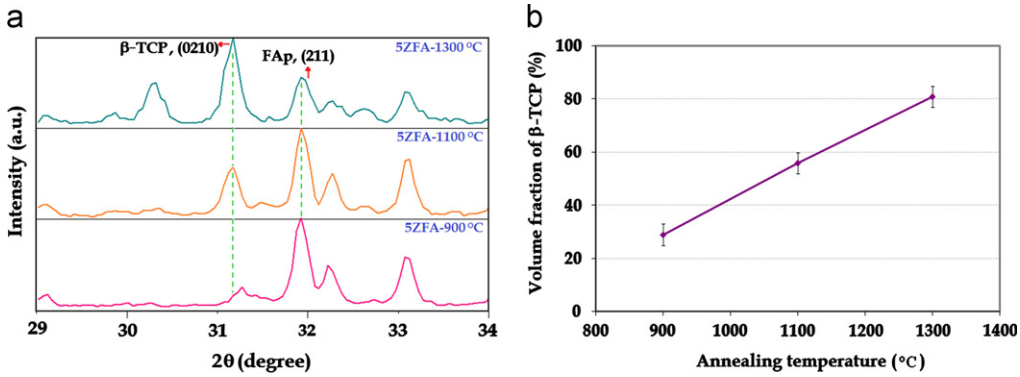

Fig. 4. (a) Magnified XRD region between $2\theta=29^{\circ}$ and 34° and (b) the volume fraction of β-TCP as a function of annealing temperature.

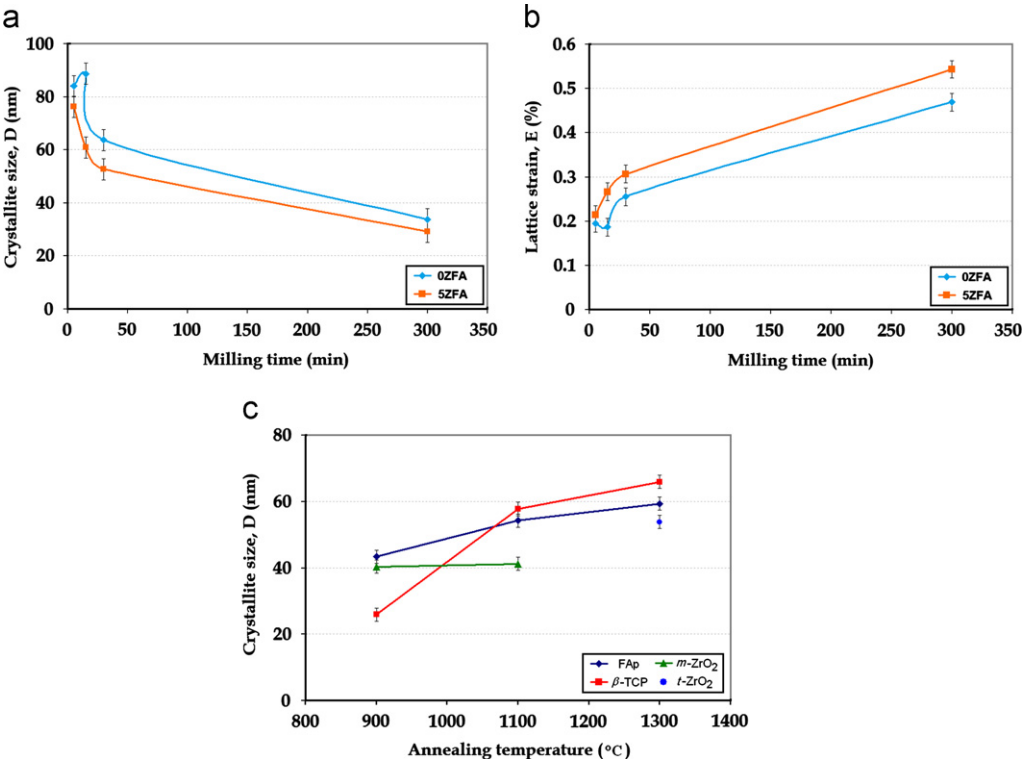

Fig. 5. Structural features of specimens (a and b) after milling, and (c) subsequent thermal treatment at 900, 1100 and 1300 °C (b).

milling up to 15 min led to a rapid increase in the crystallite size to less than 89 nm. On prolonging the milling time from 15 to 300 min, the FAp crystallite size decreased gradually from about 89 to 34 nm. The evaluation of lattice strain indicated that the lattice strain significantly decreased with mechanical activation until 15 min and then increased with further milling up to 300 min (Fig. 5b). On the other side, the crystallite size of 5ZFA specimens decreased with increasing the milling time (Fig. 5a). In opposition, the lattice strain of FAp enhanced with increasing the milling time (Fig. 5b). This phenomenon was attributed to the effect of mechanical activation on the structural features of the products. Finally, after 300 min of milling, crystallite size and lattice strain of FAp were about 29 nm and 0.543%, respectively. The results show that by choosing the total milling time to 300 min for 0ZFA samples, the crystallite size increases first and reaches a maximum at 15 min of milling and then by further increasing the milling time to 300 min, the crystallite size decreases. Also, the crystallite size of FAp in the 5ZFA samples indicates that by increasing the milling time from 5 min to 300 min, the crystallite size declines mostly after 30 min and reaches a minimum at 300 min of milling time. The obtained results showed that the crystallite size of FAp was smaller for 5ZFA samples compared to 0ZFA specimens which was due to the effect of added 5 wt% m-ZrO_2 on elevating lattice strain. The presence of m-ZrO_2 as a second phase particles changes the local dislocation

density distribution owing to strain incompatibility between the matrix and particles which may cause excessive accumulation of internal strain. This reveals the influence of the added second phase particles in accelerating grain size reduction. This result is in agreement with other references [9]. Meanwhile, the average crystallite size of the m-ZrO_2 was about 26 nm after 300 min of milling. Crystallite size of the composite nanopowders after thermal treatment between 900 – 1300 °C is presented in Fig. 5c. The sample annealed at 900 °C exhibited small grains for FAp, β-TCP and m-ZrO_2 while the samples heat treated at 1300 °C demonstrated larger grains for these phases. In fact, increasing the annealing temperature might assist grain growth although all the composite powders were comprised of nanosize crystallites.

3.1.3. Lattice parameters

The significant evidence for the incorporation of substituted anion (F^{1-}) in the apatite structure and decomposition of FAp can also be confirmed by the calculated lattice parameters for all of the samples. Comparable data of the a-axis, c-axis and the unit cell volume changes for FAp are presented in Table 1. As it can be seen in Table 1, the a-axis values for FAp in the 0ZFA and 5ZFA samples were similar to the reported values for standard FAp (#15-0876: a=9.368 Å). Similarly, there were little changes observed in the c-axis (FAp #15-0876: c=6.884 Å). On the other hand, the calculated amounts of unit cell volume demonstrated that the unit cell volume increased first and reached a maximum at 30 min of milling and then by further increasing the milling time to 300 min, the unit cell volume decreased. These variations in volume resulted mainly from increases in the (a) parameters, rather than from the (c) values and can probably be attributed to the lattice distortion of FAp during milling of the samples. According to Table 1, the volume of FAp unit cell increased after annealing between 900 and 1300 °C. These increases in volume resulted mainly from increases in the (a) parameters, rather than from the (c) values. From XRD profiles of heat treated samples, the increased tendency of FAp decomposition due to reaction with m-ZrO_2 can be explained as resulting from the removal of calcium from FAp and its dissolution into zirconia. This solid solution of calcium into the zirconia leads to its transformation to the tetragonal phase. These results are in agreement with other studies [7,9]. The removal of calcium ions from FAp involves an ion exchange reaction with ZrO^{2+} ions from the m-ZrO_2 which can occur where the surfaces of m-ZrO_2 and FAp are in contact, with minimum rearrangement of their structures. The radius of a ZrO^{2+} ion is about 0.21 nm; that of calcium is about 0.1 nm [9]. This event explains the enhanced volume of the FAp unit cell as shown in Table 1. In addition, the large ZrO^{2+} ion introduces strain into the FAp structure, accelerating the FAp decomposition process. In the zirconia, the exchange of Ca^{2+} for a ZrO^{2+} unit leads to a smaller unit cell volume and transformation of the m-ZrO_2 to t-ZrO_2 form.

3.2. FT-IR spectra

The FT-IR spectra of the 0ZFA and 5ZFA samples milled for various periods of time are shown in Figs. 6 and 7. These spectra reflect the presence of functional groups that determine the composition of the samples and the changes that occurred during the solid state process. In the FT-IR spectra of 0ZFA samples (Fig. 6), two bands relating to the vibration of

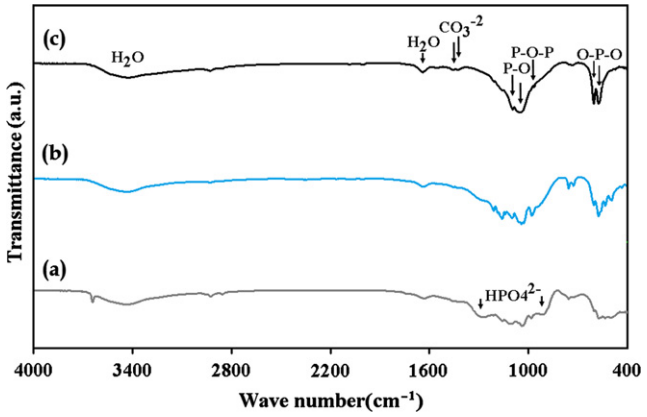

Fig. 6. FT-IR spectra of 0ZFA samples (a) before and after different milling times, (b) 5 min and (c) 300 min.

Table 1
Comparable data of the a-axis, c-axis and the unit cell volume changes for FAp.

Sample	Corresponding phases	a-axis (Å)	c-axis (Å)	Unit cell volume (Å^3)
0ZFA—5 min	FAp	9.374	6.886	1566.567
0ZFA—300 min	FAp	9.373	6.884	1565.779
5ZFA—5 min	FAp	9.357	6.870	1557.263
5ZFA—300 min	FAp	9.369	6.882	1563.987
5ZFA – 900 °C	FAp	9.375	6.884	1566.528
5ZFA – 1100 °C	FAp	9.373	6.885	1565.852
5ZFA—1300 °C	FAp	9.371	6.886	1565.564
5ZFA—1300 °C	t-ZrO_2	5.125	5.070	133.191
JCPDS #15-0876	FAp	9.368	6.884	1564.264
JCPDS #017-0923	t-ZrO_2	5.120	5.250	137.626

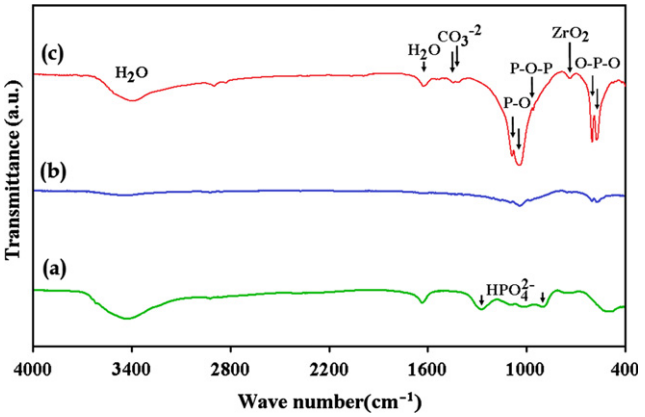

Fig. 7. FT-IR spectra of 5ZFA samples (a) before and after different milling times, (b) 5 min and (c) 300 min.

the adsorbed water in the apatite structure were detected [4]. For the sample which was milled for 300 min, a doublet appears at 1428 and 1455 cm^{-1} corresponding to v_3 and a band at 864 cm^{-1} corresponding to v_2 vibration mode of the carbonated groups. These peaks showed that FAp contained some CO_3^{2-} groups in PO_4^{3-} sites of apatite lattice (B-type substitution) [19]. The characteristic peaks of the phosphate group had four distinct asymmetrical stretching vibration modes, namely, v_1 (965 cm^{-1}), v_2 (473 cm^{-1}), v_3 (1094 and 1049 cm^{-1}), and v_4 (603 and 575 cm^{-1}) appeared in the broad spectrum. Also, the bands at 916 and 1274 cm^{-1} were assigned to the HPO_4^{2-} group vibrations [4,13], gradually diminished with increase of milling time and finally disappeared after 300 min of milling. In fact, the band at 965 cm^{-1} corresponding to the v_1 vibration of the PO_4^{3-} group appears as a result of the HPO_4^{2-} group depredation [4,13,20]. Besides the band at 727 cm^{-1}, the band at 755 cm^{-1} shows that the configuration …FHOF… is predominant [20], which confirmed the formation of FAp with acceptable purity. In FT-IR spectra of the 5ZFA samples (Fig. 7), similar bands relating to the vibration of the adsorbed water in the apatite structure were also identified. In addition, similar to previous samples (0ZFA), a doublet appears at 1429 and 1457 cm^{-1} corresponding to v_3 and a band at 865 cm^{-1} attributed to v_2 vibration mode of the carbonated groups which showed that FAp contained some CO_3^{2-} groups in PO_4^{3-} sites of apatite lattice (B-type substitution) [19]. It has been reported that this kind of apatite is more similar to biological apatite and could be more suitable for bone replacement materials [4]. The main characteristic peaks of $PO4^{3-}$ group had four distinct asymmetrical stretching vibration modes; namely v_1 (P–O–P), v_2 (P–O–P), v_3 (P–O), and v_4 (O–P–O) were clearly observed, given as follows. The v_1 and v_2 vibration peaks were observed at 965 and 473 cm^{-1}, respectively. The v_3 vibration peak was noted in the region between 1094 and 1049 cm^{-1} which was the most intensified peak among the phosphate vibration modes. The band between 603 and 575 cm^{-1} showed v_4 vibration mode of PO_4^{3-} group. Comparison of FT-IR spectra between milled samples and the starting mixture confirmed considerable changes in the system phase composition which occurred during mechanochemical process. Similar to previous sample (0ZFA), the bands at 900 and 1273 cm^{-1} were assigned to the HPO_4^{2-} group vibrations [4,13] disappeared after 300 min of milling. Furthermore, the band at 741 cm^{-1} corresponds to the vibration of ZrO_2 with small differences depending of the milling time. The FT-IR results combined with XRD findings confirmed that the formation of fluorapatite–zirconia composite nanopowders progressed in several steps.

3.3. Elemental analysis

Fig. 8 shows the EDX spectra of the 0ZFA and 5ZFA samples after 300 min of milling. EDX spectra revealed that the main elements of the samples were calcium, phosphorus, oxygen, fluorine and zirconium. The EDX of FAp crystals present in the 0ZFA and 5ZFA specimens showed a molar ratio Ca/P=1.83 and 1.72, respectively. These results illustrate that the FAp crystals are closer to the standard fluorapatite (Ca/P=1.67) [14,21]. Moreover, the EDX results confirmed that a very homogeneous distribution of components was formed after mechanical activation of both samples (0ZFA and 5ZFA), particularly after 300 min of milling. In accordance with EDX point chemical analysis, no chemically stable contaminants were detected due to the excessive adhesion of powders to the milling media. It has been shown that the polyamide-6 vial is a proper milling media to annihilate contamination problem and to achieve modified morphologies with high biomedical performance [13,14,22–24].

3.4. Morphological characteristics

In this paper, for a better understanding of the effect of mechanical activation and subsequent thermal treatment on morphological features of the samples, FE-SEM analysis were performed on the specimens. Fig. 9 shows the morphology and particle size distribution of the 0ZFA and 5ZFA samples milled for 5 and 300 min. After 5 min of mechanical activation, some large platelet or flake shape agglomerates/particles were formed in the 0ZFA sample due to the agglomerates/particles may undergo different compression and wear forces of the colliding balls (Fig. 9a). At this stage, the size distribution range of FAp particles was approximately 80 nm–1 μm. With increasing milling time up to 300 min, the particles gradually became equiaxed as were presented in Fig. 9c. The gained powders showed a cluster-like structure which was composed of several fine particles with the average size of about 55 nm. According to Fig. 9b and a considerable activation happened in the powder mixture after 5 min of milling. Since, the XRD analysis confirmed the formation of FAp–5 wt% *m*-ZrO_2 composite nanopowder after 5 min of milling; it seems that the localized heating and pressure at regions of contact between the reactant with fine grains may be an important factor for the phase formation in the activated sample for 5 min of milling [13]. By increasing milling time to 300 min,

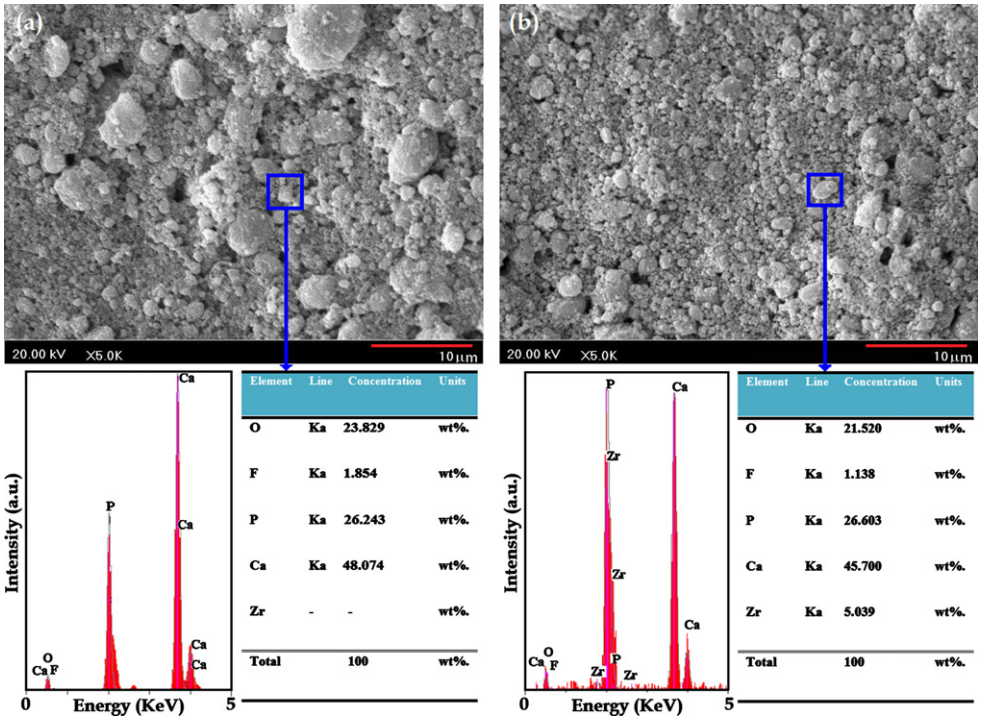

Fig. 8. EDX spectra of (a) 0ZFA, and (b) 5ZFA samples after 300 min of milling.

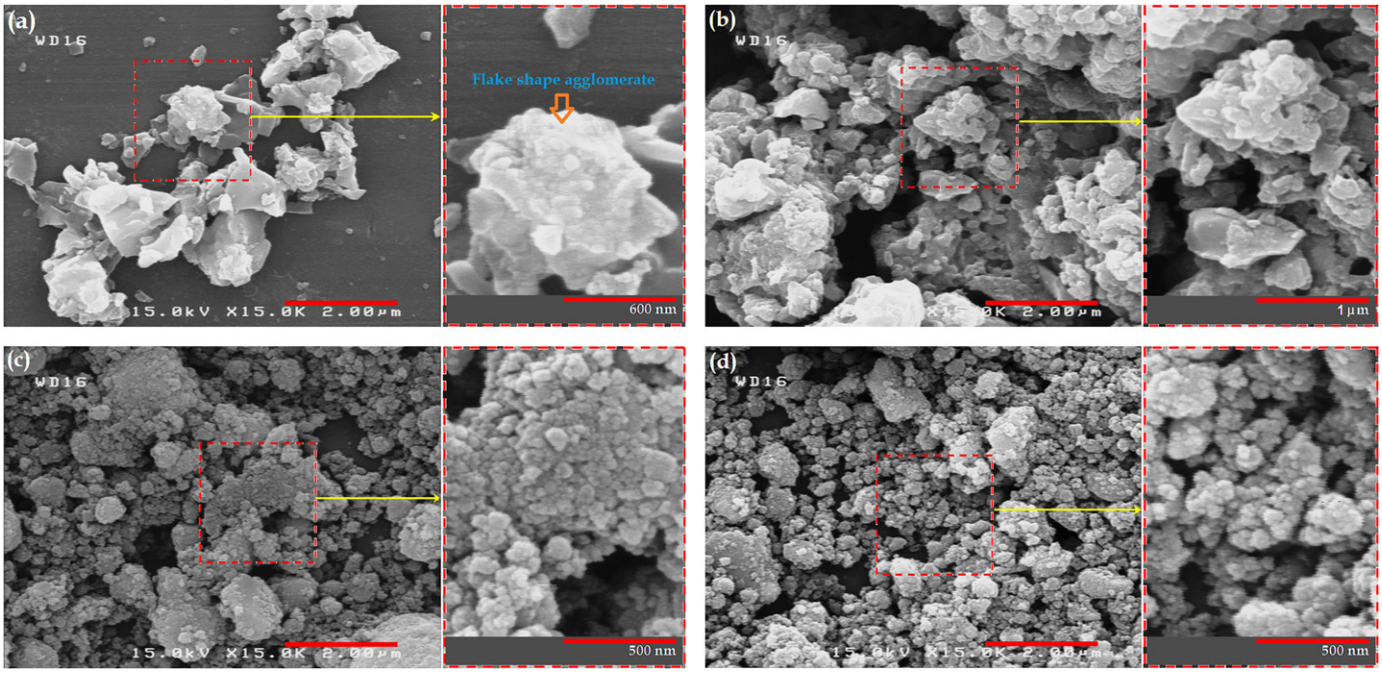

Fig. 9. FE-SEM images of the samples after different milling times: (a) 0ZFA—5 min, (b) 5ZFA—5 min, (c) 0ZFA—300 min, and (d) 5ZFA—300 min.

the rate of fracturing increased and as a result the size of powder particles decreased. At this stage, the morphology of nanoparticles was almost equiaxed with the average size of about 45 nm (Fig. 9d).

Fig. 10 shows the morphological features of 5ZFA samples annealed in the range of 900–1300 °C. These observations clearly expose distinct differences in the microstructural characteristics of the specimens. At 900 °C, the powder particles became nearly equiaxed in shape with a mean grain size of about 209 nm (Fig. 10a). When the annealing temperature increased to 1100 °C, grain growth occurred and pore free/dense microstructure was obtained (Fig. 10b). At this temperature, the microstructure showed a bimodal grain size distribution charac-

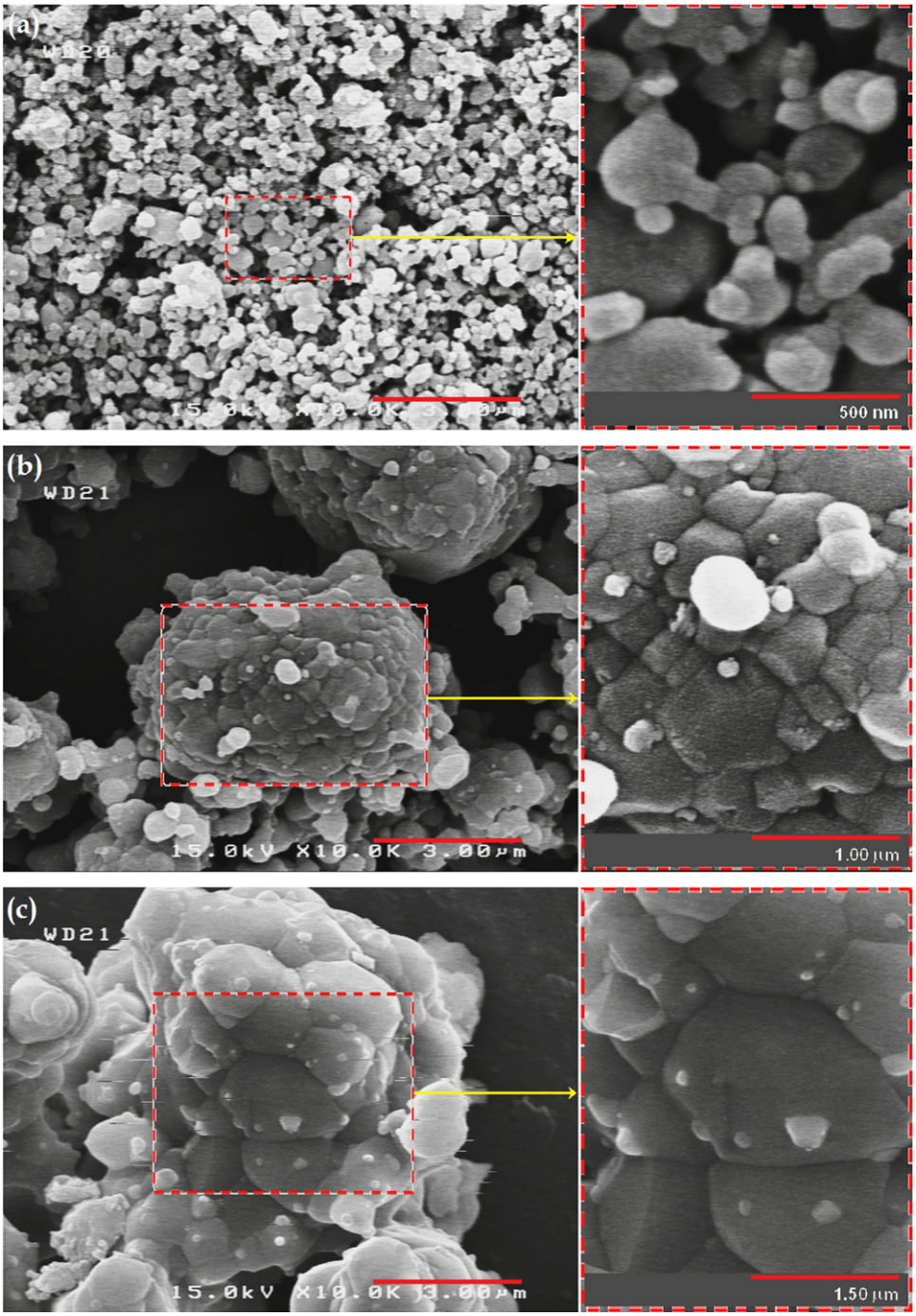

Fig. 10. Morphological features of the FAp–ZrO_2 composite nanopowders annealed at: (a) 900, (b) 1100, and (c) 1300 °C.

terized by the presence of several coarse grains (~620 nm) along with finer grains with the mean particle size of about 270 nm. The same trend is followed for the heat treated sample at 1300 °C as shown in Fig. 10c. At 1300 °C, the sample was composed of coarse grains (~2 μm) accompanied by few smaller grains (~270 nm). It should be noted that the average size of agglomeration for the sample heat treated at 1100 °C was about 6 μm, whereas the mean agglomeration size for the specimen annealed at 1300 °C was about 8 μm. The increase in the average size of agglomeration with increasing temperature may be ascribed to the coalescence of fine agglomerates.

3.5. Reaction mechanism

Fig. 11 shows the schematic formation and decomposition of fluorapatite–zirconia composite nanopowders during mechanochemical process and subsequent thermal treatment. Based on this figure and obtained data by FT-IR spectroscopy, XRD, SEM/EDX and FE-SEM analysis as

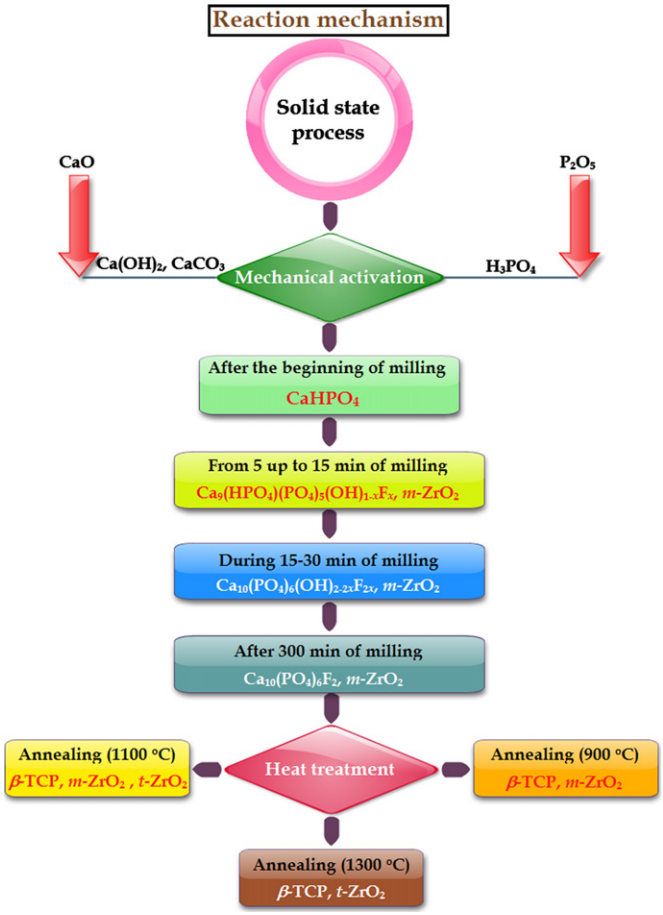

Fig. 11. Schematic formation and decomposition of fluorapatite−zirconia composite nanopowders during mechanochemical process and subsequent thermal treatment.

well as thermodynamic values which were obtained from commercial software (HSC [25]), the following reaction mechanism steps have been proposed to clarify the reactions occurring during the solid state process of CaO–P_2O_5–CaF_2–ZrO_2 system. Fundamentally, the formation of FAp–ZrO_2 composite was affected by presence of P_2O_5 in reaction mixture as a source of supply PO_4^{3-} group. This can be explained considering the hygroscopic nature of P_2O_5; so that, water adsorption from the environment causes its transformation to H_3PO_4 through the following reaction:

$$3P_2O_5+9H_2O\rightarrow 6H_3PO_4,\quad \Delta G_{298\ K}=-493.081\ kJ,\quad \Delta H_{298\ K}=-586.317\ kJ \tag{4}$$

Phosphoric acid behaves as a triprotic acid which is having three ionizable hydrogen atoms. The hydrogen ions are lost sequentially:

$$H_3PO_4\leftrightarrow H^+ + H_2PO_4^-,\quad pK_a=-\log_{10}K_a=2.12,\quad K=7.52\times 10^{-3} \tag{5}$$

$$H_2PO_4^-\leftrightarrow H^+ + HPO_4^{2-},\quad pK_a=-\log_{10}K_a=7.21,\quad K=6.23\times 10^{-8} \tag{6}$$

$$HPO_4^{2-}\leftrightarrow H^+ + PO_4^{3-},\quad pK_a=-\log_{10}K_a=12.57,\quad K=2.2\times 10^{-13}c \tag{7}$$

It should be mentioned that the reaction with starting reagents will proceed depending on the ionization stage of the H_3PO_4:

$$CaO[CaF_2]+H_3PO_4\rightarrow H^+ + H_2PO_4^- + CaO[CaF_2] \tag{8}$$

$$CaO[CaF_2]+H^+ + H_2PO_4^-\rightarrow CaHPO_4+H_2O[2HF] \tag{9}$$

$$3CaO[3CaF_2]+6H^+ + 2PO_4^{3-}\rightarrow Ca_3(PO_4)_2+3H_2O[6HF] \tag{10}$$

It appears that the dissociation of the acid pursues reaction (5) and thus the reaction of starting reagents with H_3PO_4 caused the formation of $CaHPO_4$ as an intermediate phase during mechanical activation, according to reaction (9). Furthermore, CaO is unstable and can be transformed to $CaCO_3$ or to $Ca(OH)_2$ in air.

$$CaO+H_2O\rightarrow Ca(OH)_2,\quad \Delta G_{298\ K}=-57.804\ kJ,\quad \Delta H_{298\ K}=-65.146\ kJ \tag{11}$$

$$CaO+CO_2\rightarrow CaCO_3,\quad \Delta G_{298\ K}=-130.447\ kJ,\quad \Delta H_{298\ K}=-178.175\ kJ \tag{12}$$

Therefore, similar to previous reaction (9), the reaction of $Ca(OH)_2$ and $CaCO_3$ with H_3PO_4 were also caused the formation of $CaHPO_4$ during milling as follows:

$$Ca(OH)_2 + H^+ + H_2PO_4^- \rightarrow CaHPO_4 + 2H_2O \quad (13)$$

$$CaCO_3 + H^+ + H_2PO_4^- \rightarrow CaHPO_4 + H_2O + CO_2 \quad (14)$$

Based on reactions (13) and (14), after the mixing of starting reagents mainly the following reactions were dominated:

$$Ca(OH)_2 + H_3PO_4 \rightarrow CaHPO_4 + 2H_2O,$$
$$\Delta G_{298\ K} = -138.252\ kJ, \quad \Delta H_{298\ K} = -121.163\ kJ \quad (15)$$

$$CaCO_3 + H_3PO_4 \rightarrow CaHPO_4 + H_2O + CO_2,$$
$$\Delta G_{298\ K} = -65.609\ kJ, \quad \Delta H_{298\ K} = -8.133\ kJ \quad (16)$$

After the beginning of milling:

$$CaF_2 + H_3PO_4 \rightarrow CaHPO_4 + 2HF, \quad \Delta G_{298\ K} = +68.240\ kJ,$$
$$\Delta H_{298\ K} = +93.034\ kJ \quad (17)$$

From 5 up to 15 min of milling:

$$3CaO + 3H_3PO_4 + m\text{-}ZrO_2 \rightarrow 3CaHPO_4 + m\text{-}ZrO_2 + 3H_2O$$
$$\Delta G_{298\ K} = -585.846\ kJ, \quad \Delta H_{298\ K} = -579.634\ kJ \quad (18)$$

$$6CaHPO_4 + 3CaO + xHF + m\text{-}ZrO_2 \rightarrow$$
$$Ca_9(HPO_4)(PO_4)_5(OH)_{1-x}F_x + m\text{-}ZrO_2 + (2+x)H_2O \quad (19)$$

During $15-30$ min of milling:

$$Ca_9(HPO_4)(PO_4)_5(OH)_{1-x}F_x + CaO + xHF + (1-x)H_2O$$
$$+ m\text{-}ZrO_2 \rightarrow Ca_{10}(PO_4)_6(OH)_{2-2x}F_{2x} + m\text{-}ZrO_2 + H_2O \quad (20)$$

Finally, after 300 min of milling:

$$Ca_{10}(PO_4)_6(OH)_{2-2x}F_{2x} + (2-2x)HF + m\text{-}ZrO_2 \rightarrow$$
$$Ca_{10}(PO_4)_6F_2 + m\text{-}ZrO_2 + (2-2x)H_2O \quad (21)$$

The thermodynamic feasibility of mentioned reactions was assessed from the free energy calculations. In spite of reaction (17), during milling at room temperature, reactions (4), (11), (12), (15), (16) and (18) can thermodynamically be possible to occur due to the negative $\Delta G_{298\ K}$ of reactions. In addition, negative $\Delta H_{298\ K}$ of listed reactions indicates that these reactions are exothermic, but reaction (17) is endothermic. Clearly, the occurrence of these reactions at room temperature is limited by kinetic conditions. From the point of view of thermodynamics, reaction (17) is not feasible reaction ($+\Delta G$ value); nevertheless, mechanochemical processes can enhance the feasibility of such reactions. This can be related to creation of new surfaces by reduction in the average particle size during milling, decrease in the diffusion distances by creation of lattice defects and local temperature pulses due to ball collisions [26].

It should be mentioned that some of proposed reactions mostly proceed with incomplete stoichiometry, wherein the value x defines the deviation from the complete stoichiometry within the interval (x_1; x_f); $x_1 < x < x_f$, where x_f and x_1 can have the maximum value of 1 and the minimum value of 0, respectively. Therefore, the stoichiometry for the overall reaction of mechanosynthesis will be the reaction (1). The obtained results suggest that the synthesis of FAp–ZrO_2 composite nanopowders proceeds in several steps:

(a) Phosphoric acid is formed immediately upon addition of P_2O_5 to the reaction mixture.
(b) Phosphoric acid then reacts with $Ca(OH)_2$, $CaCO_3$, CaF_2, and CaO according to reactions (15)–(18) which resulted in the formation of $CaHPO_4$ as an intermediate phase.
(c) After ball milling for 5 min, characteristic bands for HPO_4^{2-} become less and less intense and disappearing completely after 300 min which confirms the progress of mechanochemical reaction during 5 up to 300 min of milling. In fact, the band at 965 cm^{-1} corresponding to the PO_4^{3-} group appeared as a result of HPO_4^{2-} group depredation.
(d) The mechanochemical process progresses by the formation of the stoichiometrically deficient hydroxyfluorapatite [$Ca_9(HPO_4)(PO_4)_5(OH)_{1-x}F_x$] during 5 up to 15 min of milling.
(e) During 15 up to 30 min of milling, the stoichiometrically deficient hydroxyfluorapatite reacts with the remaining CaO according to reaction (20). It reveals that the CaO is still presented in our samples, as shown in the XRD profiles. In this step, the formation of $Ca_{10}(PO_4)_6(OH)_{2-2x}F_{2x}$ becomes dominant.

On the other hand, the annealing process in the range of 600–900 °C led to two important phase transformations: (a) decomposition of FAp to $Ca_3(PO_4)_2$ and CaF_2 as well as (b) transformation of m-ZrO_2 to t-ZrO_2. Therefore, the following reactions were proposed:

$$Ca_{10}(PO_4)_6F_2 \rightarrow 3Ca_3(PO_4)_2 + CaF_2 \quad (22)$$

$$m\text{-}ZrO_2 + CaF_2 \rightarrow \text{Ca-doped } t\text{-}ZrO_2 \quad (23)$$

Recalling from the above observations, it can be concluded that formation and decomposition of FAp–ZrO_2 composite nanopowders proceeded in several steps. Based on the equations, mechanochemical reactions in the system have been accelerated by an alleviated transport of the corresponding ions to the reaction zone. From above-mentioned reactions, in this process presence of water as a by-product and high energy of milling had a positive effects on the composite formation. Furthermore, adding of 5 wt% m-ZrO_2 to powder mixture had helpful result on the generation of FAp–ZrO_2 composite nanopowders with high phase purity.

4. Conclusions

The reaction mechanisms of generation and decomposition of FAp–ZrO_2 composite nanopowders were studied

after milling and subsequent thermal treatment. In the absence of m-ZrO_2, the produced FAp had the Ca/P ratio lower than stoichiometry value as a result of $Ca_2P_2O_7$ formation after 5, 15 and 30 min of milling. When the mechanical activation time was extended to 300 min, all the peaks corresponding to $Ca_2P_2O_7$ and CaO disappeared and only those belonging to FAp were detectable. In the presence of 5 wt% m-ZrO_2, ball milling up to 300 min resulted in FAp–ZrO_2 composite nanopowders with no impurity phase. The average crystallite size of FAp was smaller for the 5ZFA samples compared to 0ZFA specimens. The volume fraction of β-TCP enhanced as a result of FAp decomposition during heating at ≥ 900 °C. Results revealed that the volume of FAp unit cell increased after annealing between 900 and 1300 °C due to the ions exchange reaction. On the other hand, in the zirconia exchange of Ca^{2+} for a ZrO^{2+} unit led to the transformation of the m-ZrO_2 to t-ZrO_2 form. Based on FE-SEM observations, when the annealing temperature increased to 1100 °C, microstructure showed a bimodal grain size distribution. The same trend is followed for the sample; heat treated at 1300 °C. Moreover, the increase in average size of agglomeration with increasing temperature may be ascribed to the coalescence of fine agglomerates. The gained results suggest that the synthesis of FAp–ZrO_2 composite nanopowders progressed in several stages. In the proposed solid state procedure, presence of water as a by-product and high energy of milling had a positive effects on the formation of the composite.

Acknowledgment

The authors are grateful to research affairs of Islamic Azad University, Najafabad Branch for supporting of this research.

References

[1] S.J. Kalita, A. Bhardwaj, H.A. Bhatt, Nanocrystalline calcium phosphate ceramics in biomedical engineering, Materials Science and Engineering C 27 (2007) 441–449.

[2] M. Fini, L. Savarino, N.N. Aldini, L. Martini, G. Giavaresi, G. Rizzi, D. Martini, A. Ruggeri, A. Giunti, R. Giardino, Biomechanical and histomorphometric investigations on two morphologically differing titanium surfaces with and without fluorohydroxyapatite coating: an experimental study in sheep tibiae, Biomaterials 24 (2003) 3183–3192.

[3] Y. Chen, X. Miao, Thermal and chemical stability of fluorohydroxyapatite ceramics with different fluorine contents, Biomaterials 26 (2005) 1205–1210.

[4] M.H. Fathi, E.Mohammadi Zahrani, Mechanical alloying synthesis and bioactivity evaluation of nanocrystalline fluoridated hydroxyapatite, Journal of Crystal Growth 311 (2009) 1392–1403.

[5] I. Mayera, J.D.B. Featherstone, Dissolution studies of Zn-containing carbonated hydroxyapatites, Journal of Crystal Growth 219 (2000) 98–101.

[6] B. Viswanath, N. Ravishankar, Interfacial reactions in hydroxyapatite/alumina nanocomposites, Scripta Materialia 55 (2006) 863–866.

[7] R.R. Rao, T.S. Kannan, Synthesis and sintering of hydroxyapatite–zirconia composites, Materials Science and Engineering C 20 (2002) 187–193.

[8] F. Ben Ayed, J. Bouaziz, Sintering of tricalcium phosphate-fluorapatite composites with zirconia, Journal of the European Ceramic Society 28 (2008) 1995–2002.

[9] Z. Evis, Reactions in hydroxylapatite–zirconia composites, Ceramics International 33 (2007) 987–991.

[10] C.C. Silva, M.A. Valente, M.P.F. Graça, A.S.B. Sombra, Preparation andoptical characterization of hydroxyapatite and ceramic systems with titanium and zirconiumformed by dry high-energy mechanical alloying, Solid State Sciences 6 (2004) 1365–1374.

[11] S. Nath, R. Tripathi, B. Basu, Understanding phase stability, microstructure development and biocompatibility in calcium phosphate–titania composites, synthesized from hydroxyapatite and titanium powder mixture, Materials Science and Engineering C 29 (2009) 97–107.

[12] H.W. Kim, Y.M. Kong, Y.H. Koh, H.E. Kim, Pressureless sintering andmechanical and biological properties of fluor-hydroxyapatite composites with zirconia, Journal of the American Ceramic Society 86 (2003) 2019–2026.

[13] B. Nasiri-Tabrizi, A. Fahami, Synthesis and characterization of fluorapatite–zirconia composite nanopowders, Ceramics International (2012)http://dx.doi.org/10.1016/j.ceramint.2012.11.016.

[14] A. Fahami, B. Nasiri-Tabrizi, R. Ebrahimi-Kahrizsangi, Synthesis of calcium phosphate-based composite nanopowders by mechanochemical process and subsequent thermal treatment, Ceramics International 38 (2012) 6729–6738.

[15] J. Qian, Y. Kang, W. Zhang, Zh. Li, Fabrication, chemical composition change and phase evolution of biomorphic hydroxyapatite, Journal of Materials Science: Materials in Medicine 19 (2008) 3373–3383.

[16] Y.M. Sung, D.H. Kim, Crystallization characteristics of yttria-stabilized zirconia/hydroxyapatite composite nanopowder, Journal of Crystal Growth 254 (2003) 411–417.

[17] I. Manjubala, M. Sivakumar, In-situ synthesis of biphasic calcium phosphate ceramics using microwave irradiation, Materials Chemistry and Physics 71 (2001) 272–278.

[18] W. Hui, S. Sen, W. Yao, L. Chang-shun, S. Jian, CaF_2-doped ZrO_2: a base catalyst for synthesis of dimethyl carbonate, Journal of Shanghai University 14 (2010) 281–285.

[19] J.P. Lafon, E. Champion, D. Bernache-Assollant, Processing of AB-type carbonated hydroxyapatite $Ca_{10-x}(PO_4)_{6-x}(CO_3)_x(OH)_{2-x-2y}(CO_3)_y$ ceramics with controlled composition, Journal of the European Ceramic Society 28 (2008) 139–147.

[20] I. Nikcevic, V. Jokanovic, M. Mitric, Z. Nedic, D. Makovec, D. Uskokovic, Mechanochemical synthesis of nanostructured fluorapatite/fluorhydroxyapatite and carbonated fluorapatite/fluorhydroxyapatite, Journal of Solid State Chemistry 177 (2004) 2565–2574.

[21] I. Cacciotti, A. Bianco, M. Lombardi, L. Montanaro, Mg-substituted hydroxyapatite nanopowders: synthesis, thermal stability and sintering behavior, Journal of the European Ceramic Society 29 (2009) 2969–2978.

[22] B. Nasiri-Tabrizi, P. Honarmandi, R. Ebrahimi-Kahrizsangi, P. Honarmandi, Synthesis of nanosize single-crystal hydroxyapatite via mechanochemical method, Materials Letters 63 (2009) 543–546.

[23] R. Ebrahimi-Kahrizsangi, B. Nasiri-Tabrizi, A. Chami, Characterization of single-crystal fluorapatite nanoparticles synthesized via mechanochemical method, Particuology 9 (2011) 537–544.

[24] A. Fahami, R. Ebrahimi-Kahrizsangi, B. Nasiri-Tabrizi, Mechanochemical synthesis of hydroxyapatite/titanium nanocomposite, Solid State Sciences 13 (2011) 135–141.

[25] Outokumpu HSC Chemistry® Version 5.1, Outokumpu Research Oy Information Service, Pori, Finland, 2002, 〈http://www.outokumpu.com/hsc〉.

[26] P. Balaz, Mechanochemistry in Nanoscience and Minerals Engineering, 1st ed., Springer, Berlin, Heidelberg, 2008.